

# 3D conformation of a flexible fiber in a turbulent flow

Gautier Verhille · Adrien Bartoli

Received: date / Accepted: date

**Keywords** Turbulent flows · Fibers in turbulence · Epipolar geometry

**PACS** 47.27.-i · 42.30.Tz

**Abstract** A growing number of studies is devoted to anisotropic particles in turbulent flows. In most cases the particles are assumed to be rigid and their deformations are neglected. We present an adaptation of classical computer vision tools to reconstruct from two different images the 3D conformation of a fiber distorted by the turbulent fluctuations in a von Kármán flow. This technique allows us notably to characterize the fiber deformation by computing the correlation function of the orientation of the tangent vector. This function allows us to tackle the analogy between polymers and flexible fibers proposed by Brouzet *et al.* (Phys. Rev. Lett. **112**(7) 074501 (2014)). We show that this function depends on an elastic length  $\ell_e$  which characterizes the particle flexibility, as is the case for polymers, but also on the fiber length  $L$ , contrary to polymers.

## 1 Introduction

The transport of fibers in turbulent flows is a key point in several applications such as the paper and textile industries [15, 22] and polymer processing [10]. In all these cases, the quality of the final product depends on the fiber orientation statistics (homogeneity and isotropy

mainly). The dynamics of fibers in turbulent flows is also relevant in environmental sciences. Indeed phytoplanktons play a key role in the ocean by producing organic matter and oxygen from the  $\text{CO}_2$  dissolved in water. It is known that the rotation rate influences the chemotaxis of these organisms [18] and that the shape of a particle influences its rotation rate in a shear flow [9].

Since 2010, an increasing body of work has been devoted to the dynamics of anisotropic particles in turbulence. In theoretical works on anisotropic particles, the particle inertia is generally neglected. Then, the particles are assumed to have the same density as the carrying fluid and to be smaller than the Kolmogorov scale  $\eta_K$ , *i.e.* the smallest spatial scale of the flow. In that case, the particles can be modeled as point particles with a given aspect ratio  $\Lambda$  ( $\Lambda \sim \infty$  for thin rod and  $\Lambda = 0$  for thin discs). Thus the advection and the orientation dynamics are decoupled. While the advection is simply the one of a tracer following flow streamlines, the rotation dynamics is determined by the local shear according to Jeffery's work [11]. As a consequence, fibers are preferentially aligned with the vorticity [27, 5]. The 'point-fiber' approach has also been used in various numerical works such as in inhomogeneous and anisotropic turbulence to investigate the influence of walls on the fiber dynamics [20]. The first measurement of the orientation dynamics of cylindrical particles in a turbulent flow was made by Parsa *et al.* [25]. They used 4 high speed cameras to reconstruct the particle orientation in space. Another technique was used by Byron *et al.* [3] with hydrogel particles seeded with small fluorescent beads. They could determine the global rotation rate of discs and rods with a classical Particle Image Velocimetry (PIV) algorithm. For more complex 3D objects, Marcus *et al.* [21] proposed to determine the orientation with a stereo-matching method, by minimizing

---

Gautier Verhille  
Aix Marseille Université, CNRS, Centrale Marseille, IRPHE  
UMR 7342, 13384, Marseille, France  
E-mail: gautier.verhille@irphe.univ-mrs.fr

Adrien Bartoli  
ISIT UMR 6284 CNRS, Université d'Auvergne Batiment 3C, Faculté de Médecine 28 place Henri Dunant, BP 38, 63001 Clermont-Ferrand, France

the error between the projection of synthetic particles and experimental images. Zimmermann *et al.* [35] also used this technique to measure the rotation rate of a large painted spherical particle. The recorded pattern was then compared to a previous set of images to determine the particle orientation.

In all these works, the particles are assumed rigid. However, it is known that increasing the aspect ratio of a particle increases its flexibility. This raises the question of the influence of the deformation on the transport. In a previous paper, we showed that the flexibility of a fiber cannot be neglected if its length is longer than an elastic length  $\ell_e = (EI)^{1/4}/(\rho\eta\epsilon)^{1/8}$ , where  $EI$  is the bending modulus of the fiber,  $\rho$  and  $\eta$  the fluid density and viscosity, and  $\epsilon$  the power injected in the turbulence [2]. This length is defined by the equilibrium between the injected power in turbulence and the power needed to bend a fiber. We also proposed an analogy between a fiber distorted by the turbulent fluctuations and a semiflexible polymer in thermal equilibrium in a good solvent. Measuring the 3D conformation of a fiber is a key point to test this analogy. But it may also be useful to determine some flow properties which can be difficult to estimate otherwise. For instance, the injected power in the turbulence  $\epsilon$  can be known from the measurement of the elastic length  $\ell_e$ .

We present an experimental technique from 3D computer vision to reconstruct the 3D conformation of a fiber. By carefully adapting the method to our images we are able to determine the conformation of flexible fibers in a turbulent flow, from the images of two cameras. In this paper, we restrict ourselves to fiber lengths smaller or of the order of the flow integral scale and to a single elastic length which lies in the inertial range. We focus on the evolution of the correlation function of the orientation of the tangent vector along the fiber, which is a key quantity to understand the analogy with polymers. We will see that the shape of this function is similar in both cases, but that the particle length plays a role for fibers contrary to polymers. The experimental setup is described in the second section. The third section is focused on the 3D reconstruction technique and the fourth section presents the validation of the technique. Finally, our results are presented and discussed in the last section, before the conclusions.

## 2 Experimental setup

Turbulence is generated in a von Kármán flow by the counter-rotation of two impellers [28, 35]. Whereas most experiments are done in a cylindrical geometry, the flow is here confined in a cubic box of  $20 \times 20 \times 20 \text{ cm}^3$  to reduce optical distortions, *cf.* figure 1. The impellers have

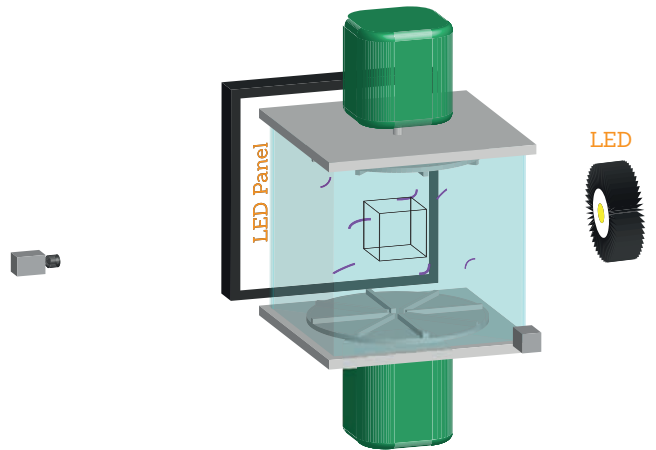


**Fig. 1** Schematic of the experimental setup. The black cube in the center of the vessel materializes the reconstruction volume where the fiber conformation is measured.

a diameter of  $2R=17 \text{ cm}$  and are fitted with 6 straight blades with height  $0.5 \text{ cm}$ . The distance between the two impellers is  $17 \text{ cm}$ . They are set in motion by two  $350 \text{ W}$  asynchronous motors at a constant rotation frequency  $F$  in the range  $[1;30] \text{ Hz}$ . All the results presented here have been measured in water at ambient temperature ( $\rho = 10^3 \text{ kg.m}^{-3}$ ,  $\eta = 10^{-3} \text{ Pa.s}$ ) with a rotation frequency of  $15 \text{ Hz}$ . The energy dissipation rate  $\epsilon$  is then around  $6 \text{ W.kg}^{-1}$ . This flow has been extensively used to study different problems in turbulence such as Lagrangian turbulence (see for instance [30] and references therein), dynamo instability [23] or quantum turbulence [29]. The mean flow is composed of two toroidal cells with a large azimuthal shear at the center and two poloidal recirculation cells due to the centrifugal forces near the impellers [16, 14]. If the small scales of the flow are expected to be isotropic due to the high Reynolds number, the large scales are anisotropic due to the stretching induced by the poloidal cells [33, 24]. The influence of the flow anisotropy is beyond the scope of this study and will be addressed in future work. It is known that the turbulence homogeneity is fairly good close to the stagnation point and decreases as one approaches the impellers. That is why the reconstruction volume is a cube with approximately  $6 \text{ cm}$  side length centered at the stagnation point of the flow (see the black cube in figure 1).

As discussed in the introduction, the fiber deformations are important when the fiber length  $L$  is larger than the elastic length  $\ell_e$ . Due to the size of the reconstruction volume we restrict ourselves to fiber length smaller than  $L_{max} = 5 \text{ cm}$ . Then, to maximize the deformation, we have to reduce the elastic length  $\ell_e = (EI)^{1/4}/(\rho\eta\epsilon)^{1/8}$ . Working with water at a rotation frequency of  $15 \text{ Hz}$  determines the denominator. Then

the only free parameter to minimize this characteristic length is the bending modulus, *i.e.* the Young modulus  $E$  and the fiber diameter  $d$  (the area moment of inertia  $I$  is proportional to  $d^4$ ). Softer materials with very low Young modulus such as hydrogel are generally fragile. They cannot be used to cast fibers as they would be destroyed when hitting an impeller. We found a good compromise with the silicone EC00, from Esprit Composite, which has a Young modulus  $E = 40 \pm 15$  kPa. Even if this uncertainty is relatively large it does not affect the elastic length significantly as it scales as  $E^{1/4}$ . Then the uncertainty on the elastic length is of the order of 10 %. Since this silicone is very extensible (more than 400 % of deformation before breaking), fibers are not broken when an impact occurs. This translucent silicone has been dyed with a manganese colorant powder (particle size between 1-2  $\mu\text{m}$ ) to improve the contrast for the particle detection. To make fibers the silicone is first molded in a straight laiton tube with a diameter of 600  $\mu\text{m}$  and then cut to the desired length, here between 1 and 5 cm. We have checked the fiber diameter on several fibers with a microscope and found  $d = 622 \pm 13$   $\mu\text{m}$ . With these properties, the estimated elastic length  $\ell_e$  is around  $3.4 \pm 0.3$  mm which is nearly 1/3 of the length of the shortest fibers. One can then expect that all fibers will be greatly distorted by the flow. As the silicone density is 1.03, the fiber settling speed is of the order of 1  $\text{cm.s}^{-1}$ . This velocity has to be compared to the flow speed which is of the order of 1  $\text{m.s}^{-1}$ . Therefore buoyancy effects can be neglected in the problem. Finally, to avoid inter-particle interactions the total volume concentration of fibers is around 0.002 % (so between 3 and 20 fibers depending on their length).

Since this paper focuses on the statistics of the fiber deformations and not on its dynamics, the use of high speed cameras is not necessary. Furthermore, to converge the statistics with less data, the image acquisition rate is low (a few images per second) to record uncorrelated conformations. However, the presented technique could be applied directly to dynamical problems such as the relaxation of the elastic strain or the existence of elastic waves propagating along the fiber. Two IDS UI-5240CP 1.3 Mpixels cameras with 20 mm lens are used to film the fibers in the flow at two different angles. The images are then processed with Matlab to determine the 3D shape of the fiber. To increase the contrast we used back-lighting with a LED-panel and a LED spot put behind diffusers. These light sources allow us to image fibers with an exposure time of 0.3 ms, chosen to avoid motion blur, and at a frequency of 5 images per second. This ensures that images are uncorrelated as the acquisition rate is 3 times smaller than

the rotation frequency of the impellers. The angle between the two axes of the cameras is nearly  $90^\circ$  and is determined precisely during the calibration process described in section 3.1.

### 3 3D reconstruction of the fiber conformation

#### 3.1 Principle

We intuitively know that given two images, one can reconstruct the observed 3D structure. This intuition is based on the principle of triangulation, whereby the sightlines associated to two corresponding points, one in each image, meet in the 3D space where the sought 3D point lies. This intuition forms the backbone of 3D computer vision, and has been formalized and thoroughly studied in the past few decades [8,6]. 3D computer vision has numerous applications, such as depth perception in computer-aided surgery [19].

*Modeling one camera.* The most popular camera model used in 3D computer vision is the so-called pin-hole camera. It abstracts the sensor and lens forming the camera by a simple plane, onto which the image is formed by intersecting a line joining the 3D point and the center of projection of the camera. Optical distortions, especially radial and tangential distortion, are then modeled directly in the image space. In the pin-hole model, a camera has 6 extrinsic and 5 intrinsic parameters. The extrinsic parameters give the position and orientation of the camera in space and are represented by a 3D rotation  $R$  and translation  $t$  in some world coordinate frame. The intrinsic parameters give the focal length  $f$  of the camera, the principal point (the orthogonal projection of the center of projection onto the image plane) with coordinates  $c_x, c_y$  and the skewness  $\tau$  and aspect ratio  $\alpha$  of the pixels. They are held in an upper triangulation  $3 \times 3$  matrix  $K$  whose bottom-right entry is fixed to one:

$$K = \begin{pmatrix} \alpha f & \tau & c_x \\ 0 & f & c_y \\ 0 & 0 & 1 \end{pmatrix}. \quad (1)$$

As will be seen shortly, this representation allows one to easily project 3D points to the image using homogeneous coordinates. More precisely, let  $i \in \{1, 2\}$  be the camera index, we have the extrinsic parameters as  $R_i, t_i$  and the intrinsic parameters as  $K_i$ . We now define the  $3 \times 4$  projection matrix  $P_i$  as:

$$P_i \propto K_i \begin{pmatrix} 1 & 0 & 0 & 0 \\ 0 & 1 & 0 & 0 \\ 0 & 0 & 1 & 0 \end{pmatrix} S_i, \text{ with } S_i = \begin{pmatrix} \begin{matrix} \text{---} & \text{---} & \text{---} & \text{---} \\ | & & & | \\ | & R_i & |t_i| & | \\ | & & & | \\ \text{---} & \text{---} & \text{---} & \text{---} \end{matrix} \\ 0 & 0 & 0 & 1 \end{pmatrix}. \quad (2)$$

The proportionality arises from the use of homogeneous coordinates. In that system of coordinates two points  $Q_1(X_1, Y_1, Z_1, H_1)$  and  $Q_2(X_2, Y_2, Z_2, H_2)$  are identical ( $Q_1 \propto Q_2$ ) if:

$$(X_1, Y_1, Z_1, H_1) = \lambda(X_2, Y_2, Z_2, H_2), \lambda \in \mathbb{R}^*. \quad (3)$$

For a 3D point whose world coordinates are  $(X, Y, Z)^\top$ , we construct its homogeneous coordinates, defined up to scale, as  $(X, Y, Z, 1)^\top$ . The advantage of these coordinates is that the projection operation is then simply defined as  $q_i \propto P_i Q$ , where  $q_i$  represents the homogeneous coordinates of the projected point in image  $i$ .

*Modeling two cameras.* The geometry of two cameras is specifically called the epipolar geometry [13]. For the pin-hole camera model, the epipolar geometry is represented by the  $3 \times 3$  fundamental matrix  $F$ . This matrix can be constructed from the two projection matrices  $P_1, P_2$ . Given a point with homogeneous coordinates  $q_1$  in the first image, the fundamental matrix associates the homogeneous coordinates of a line  $l_2 \propto F q_1$  to it in the second image. This line is called the epipolar line, and represents the projection of the sightline of  $q_1$  for the first camera into the second camera. It is obvious that the corresponding point  $q_2$  of  $q_1$  in the second image must lie on  $l_2$ . We thus have the following algebraic constraint, called the fundamental equation:  $q_2 \cdot F q_1 = 0$ . We will use this constraint in the next section to match the two images of a fiber, finding corresponding points by intersecting the fiber's detected image curve with epipolar lines. The epipolar lines can obviously be constructed in the first image from the second image, and this is done by using  $l_1 \propto F^\top q_2$ .

*Calibrating a pair of cameras.* The process of calibration determines the intrinsic and extrinsic parameters of the two cameras, from which the two projection matrices  $P_1$  and  $P_2$  are formed, as well as the fundamental matrix  $F$ . Calibration is done by showing the camera an object with known structure. In practice, the calibration object is constructed by printing a checkerboard pattern using a standard laser printer, which is then plasticized to make it waterproof and to increase its rigidity. Several image pairs of the calibration object are recorded with various orientations, and calibration is solved by Bouguet's method [1]. This process also estimates the radial and tangential distortion parameters, which can be neglected in our case. These will be systematically used to 'undistort' any image collected by the cameras from then on. In practice, it is important that the image pairs of the calibration object are recorded in situ. Indeed, this will guarantee that the calibration is valid where it needs to be, in other words,

where we will need to reconstruct the fibers' 3D conformation. It is also important because our experimental setup has two interfaces, between air and Plexiglas, and Plexiglas and water. This raises the question of adapting the pin-hole and epipolar models to this specific configuration, as was studied in [4]. It was however showed in a recent paper that calibrating in situ naturally adapts the models' parameters to cope with this case very well, especially for medium field-of-view cameras [31].

*Triangulating points.* We are now back to our initial intuition that 3D points can be reconstructed by intersecting two corresponding sightlines from cameras with distinct centers of projection. Concretely, triangulation is the process of finding  $Q$  from  $q_1, q_2, P_1, P_2$ . The camera matrices  $P_1, P_2$  were found by calibration, and the corresponding points  $q_1, q_2$  are found by the matching process described in the next section. Algebraically, the triangulation constraints are written as  $q_1 \propto P_1 Q$  and  $q_2 \propto P_2 Q$ . One notices that each projection gives two constraints (as the predicted image point  $P_i Q$  must match the two coordinates of the measured image point  $q_i$ ), and so a total of four constraints for the two images, but that we have only three unknowns in the 3D point  $Q$ . Geometrically, this is because one has to intersect the two sightlines, which may not meet. The most successful approach is to find the 3D point whose image projections are closest to the measured image points. This problem has an analytical solution which was given in [7].

### 3.2 Fiber reconstruction

This section is devoted to the description of how the 3D fiber conformation is determined from two images. In elasticity, the deformation of a slender object is defined by its neutral line. For an homogeneous cylinder, as is the case here, the neutral line corresponds to the center of the cross section. To determine the position of this line, two approaches are possible. The first one consists in reconstructing directly the fiber centerline by an estimation in each image of its projection, and a triangulation of these points. In the second method, the fiber edges are determined in each image and then triangulated in space. The neutral axis is then determined from the position of the edge points in space. Both techniques have been tested and give similar results for weakly distorted fibers. However if one projection of a fiber intersects itself or presents a large curvature, the approach based on the centerline frequently gives inaccurate results preventing the fiber reconstruction. For these cases the edge technique seems more robust.

We will thus only discuss the results obtained with this method in the following.

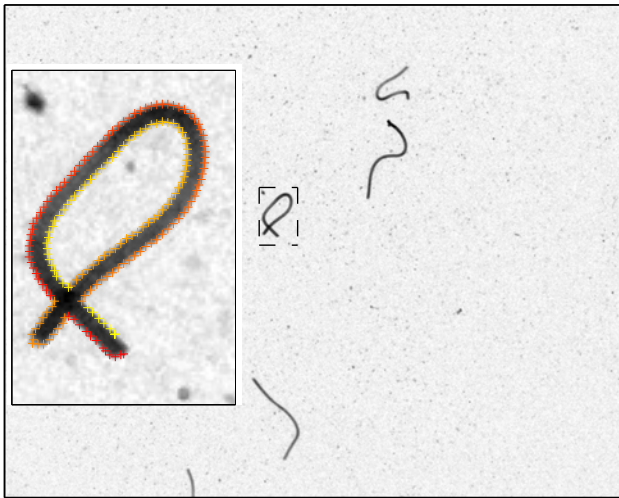


**Fig. 2** Raw images of distorted fibers in a turbulent flow. The result of the contour detection and of its orientation is presented in the inset where the crosses represent the edge points and the color, from red to yellow, represents the curvilinear coordinate (we display only one half of the points for clarity).

First, for each image, the edge coordinates are determined to sub-pixel precision using a Matlab function developed by Trujilo *et al.* [32]. This routine returns the point coordinates and the local normal vector to the edge. Each fiber is then individualized by connecting each point to its nearest neighbors. If two fibers intersect on an image they are considered as a single object after this step. Then, for each object, the fiber extremities are determined using the approach given in Lee [12] and matched from one image to the other. The edges are then oriented starting from the matched extremities in order to define a curvilinear coordinate system. To define the orientation one starts from the extremity and moves from closest neighbor to closest neighbor. This is not possible if there is an overlap of two parts of the same fiber or of two different fibers. To overcome this, we calculate the angle between the mean tangent vector calculated over the last 10 points and the vector linking the current point to its closest neighbor. If this angle is larger than some maximal value, we look for the closest point which is in the direction of the mean tangent vector and with the local normal vector aligned with the mean local normal vector calculated over the last 10 points. An illustration of the sorting of the edge points is presented in figure 2. Then each point of the edge of the fiber in image 1 is matched with the fiber edge points in image 2. Since the fiber is distorted, the epipolar line may intersect the contour at several locations.

However, since the contour is oriented it is possible to eliminate false matched points by moving from closest neighbor to closest neighbor in image 1. In that case the matching point is the closest point to the previous point in image 2.

Once we found the two points  $q_1$  and  $q_2$  on each image, we determine the 3D coordinates of point  $Q$  by triangulation. At the end of this process, we obtain a set of 3D data points representing the fiber. We then need to define the centerline coordinates. First the curvilinear coordinate  $s$  is defined for each points  $Q$  by the length of the shortest path between  $Q$  and the matched extremity used previously. This shortest path is determined by making a graph from the point coordinates defining the weight of each link by the distance between points. Links larger than the fiber diameter are removed in order to isolate each fiber. Then the centerline coordinate is found by fitting the data points with a cubic spline function. The smoothing parameter is chosen so that the maximum curvature of the reconstructed fiber does not exceed the inverse of the fiber diameter, as is the case in linear elasticity.

### 3.3 Validation

In practice a fiber might not be entirely in the volume seen by both cameras. In that case, only a part of the fiber can be reconstructed. It is not possible to use this fiber for the statistics as the fit imposes that the fiber curvature is equal to zero at the fiber extremities. To eliminate these data, we only keep fibers with an estimated length  $L_e$  of the order of the real fiber length  $L$ , in practice  $L_e = L \pm 10\%$ .

An illustration of the reconstruction is represented in figure 3 where the plain line is for the fitted curve and the scattered data for the raw data points. Note that for clarity, the distance between the raw data points and the fitted curve has been multiplied by 2. The validity of the reconstruction can be first emphasized by comparing the estimated length  $L_e$  with the fiber length  $L$ . It has to be noticed that the way fibers are manufactured gives an uncertainty on  $L$  of the order of 1 mm. One

Fiber length: $L$ [cm]	1	2	3	5
Estimated length: $\langle L_e \rangle$ [cm]	1.01	1.92	2.90	5.16
Fluctuation rate: $L_e^{rms}/\langle L_e \rangle$ [%]	3.8	3.6	3.2	3.0
Number of conformations	8868	1501	791	296

**Table 1** Comparison of the measured length and the fluctuation rate for all fiber length. The last row indicates the number of fibers used to compute the different presented statistics.

can see in table 1 that the number of fibers used for av-

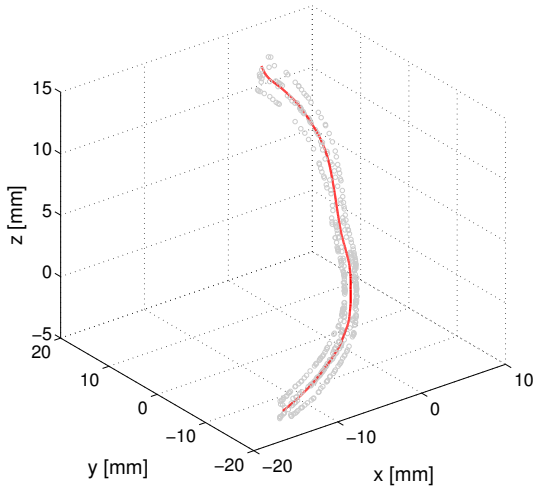


**Fig. 3** Exemple of fiber reconstruction: gray points correspond to raw data from the 3D reconstruction and the red curve is the cubic spline fit. Exemple of fiber reconstruction: the gray points correspond to raw data from the 3D reconstruction and the red curve is the cubic spline fit. For clarity, nearly 70 % of raw data points were removed randomly and the distance between the centerline and the data was multiplied by 2.

eraging depends on the fiber length. There are two reasons for that. First, the fiber concentration was smaller for long fibers to facilitate the fiber reconstruction and prevent the fiber interaction. Then, longer fibers were trapped close to the impellers more frequently, as observed for a large rigid sphere by Machicoane *et al.* [17]. Therefore, longer fibers enter in the reconstruction volume less frequently. However, we have checked that the amount of conformation was enough to converge the different statistics we present in each cases. In table 1, we can also see that the estimation of the mean values of the estimated length  $\langle L_e \rangle$ , where  $\langle \cdot \rangle$  stands for an ensemble average and the fiber length are equal within the manufactured precision. This result may be trivial as only fibers in the range  $[0.9 ; 1.1]L$  are selected for the analysis. However the distribution of the measured length is strongly peaked. This is shown by the value of the ratio of the standard deviation over the mean of the estimated length  $L_e^{rms} / \langle L_e \rangle$  which is nearly twice as small as the one of a randomly distributed variable. This also shows that, as for laminar flows, the stretching of the fiber is negligible as compared to the bending [26] and that the fiber can be considered as inextensible.

In addition, the technique used here allows us to determine the fiber diameter. Indeed, as the two camera axes are perpendicular, the edges of the projec-

tion of one image correspond to the midline of the fiber projection in the second image. Then the triangulation of the intersection of the epipolar line with the fiber edge defines a square with side length equal to  $d$ , see figure 4. Then the fiber diameter is mea-

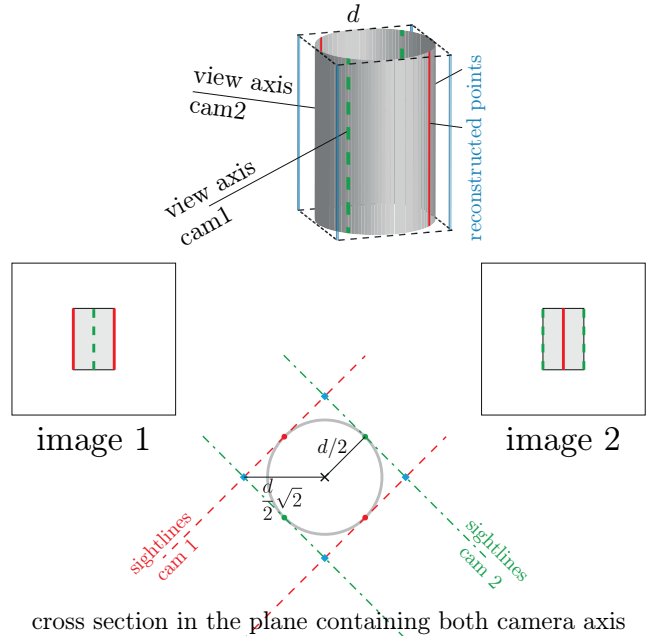


**Fig. 4** Triangulation of points from the edges of a cylinder. The red (resp. green) line represents the edges measured in image 1 (resp. 2). The triangulated points are at the intersection of the sightlines from cameras 1 and 2. As shown at the bottom of the image, they define a square tangent to the cylinder with side length equal to  $d$ .

sured by determining the distance between the reconstructed points and the fitted line. We found here  $d_m = 626 \pm 30 \mu\text{m}$ . As mentioned in section 2, the fiber diameter has been measured independently with a microscope to  $d = 622 \pm 10 \mu\text{m}$ . These two measurements are in very good agreement.

In this section we have shown that the reconstructed points are at a distance  $d/\sqrt{2}$  of the neutral line fitted with the spline function. We have also seen that the length of the fitted spline is close to the real fiber length. These observations validate the reconstruction process. We now focus on the evolution of the tangent vector along the fiber.

## 4 Results and discussion

In Brouzet *et al.* [2], an analogy between a wormlike chain polymer and a flexible fiber in a turbulent flow has been drawn. Indeed the evolution of the norm of the

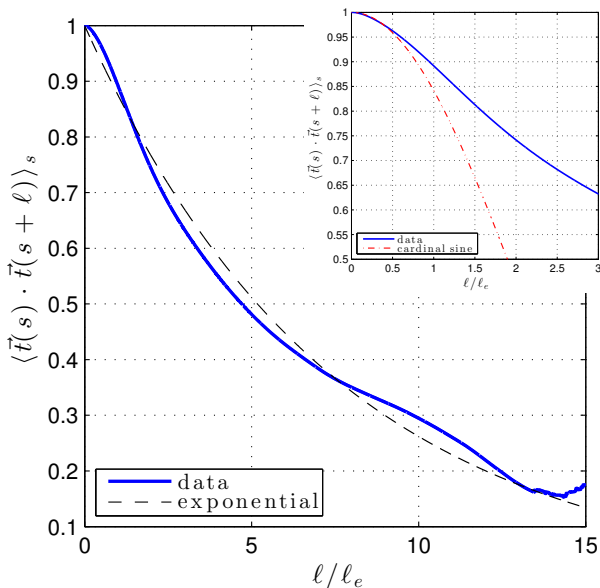


**Fig. 5** Evolution of the correlation function for the experimental data in plain (blue) line, the best exponential fit (black, dashed line). In the inset, zoom for small  $\ell$  of the correlation function (plain line) and the dashed dotted line represents the cardinal sine function  $\sin(x)/x$ , cf. text for details.

end to end vector  $\mathbf{R}_e$ , linking the two extremities, as a function of the fiber or polymer length seems similar in both cases. In the wormlike chain model [34] this norm depends on two independent parameters, the polymer length  $L$  and the persistence length  $l_p$ :

$$\langle \mathbf{R}_e^2 \rangle = 2Ll_p - 2l_p^2 \left(1 - e^{-L/l_p}\right). \quad (4)$$

The persistence length  $l_p$  is related to the polymer rigidity and is defined by  $EI/l_p = kT$  where  $EI$  is the bending modulus and  $kT$  the thermal energy.

In fact in polymer theory, this relation is an integral relation and is derived from the correlation function of the orientation of the tangent vector:

$$\mathcal{C}(\ell) = \langle \mathbf{t}(s) \cdot \mathbf{t}(s + \ell) \rangle_s = e^{-\ell/l_p}. \quad (5)$$

Here  $\mathbf{t}$  is the tangent vector (with  $\mathbf{t} \cdot \mathbf{t} = 1$ ),  $s$  and  $\ell$  are 2 curvilinear coordinates and  $\langle \cdot \rangle_s$  represents a double averaging process over realizations and over the curvilinear coordinate  $s$ . We propose to measure this correlation function for different fiber lengths in the turbulent von Kármán flow described earlier. The results are then compared to the wormlike chain prediction.

We first focus on the correlation function for the longest fibers ( $L = 5$  cm). This function is presented in figure 5 where the distance  $\ell$  has been normalized by the elastic length scale  $\ell_e$ . In this graph the experimental curve (plain blue line) is compared to the exponential law predicted for wormlike chain polymers,

cf. equation (5). The global evolution is well captured by this prediction with a persistence length  $l_p \simeq 7.5\ell_e$ . However the inset of figure 5 shows that at short length  $\ell$  the evolution of the experimental curve is quadratic ( $\mathcal{C}(\ell) \sim 1 - \alpha\ell^2$ ) whereas for an exponential law, the evolution is linear ( $\exp(-\ell/l_p) \sim 1 - \ell/l_p$ ).

In fact, one can easily show that this linear behavior is not possible either for fibers or for wormlike chains. Indeed the Taylor expansion of the correlation function gives:

$$\begin{aligned} \langle \mathbf{t}(s) \cdot \mathbf{t}(s + \ell) \rangle &\simeq \langle \mathbf{t}(s) \cdot \mathbf{t}(s) \rangle + \ell \langle \mathbf{t}(s) \cdot \partial_s \mathbf{t}(s) \rangle + \\ &\frac{\ell^2}{2} \langle \mathbf{t}(s) \cdot \partial_{ss} \mathbf{t}(s) \rangle + \frac{\ell^3}{6} \langle \mathbf{t}(s) \cdot \partial_{sss} \mathbf{t}(s) \rangle + \mathcal{O}(\ell^4). \end{aligned} \quad (6)$$

By definition the tangent vector is normalized. Thus it has to verify the two relations  $\mathbf{t} \cdot \mathbf{t} = 1$  and  $\partial_s(\mathbf{t} \cdot \mathbf{t}) = 0$ . Therefore for small  $\ell$ , the correlation of the orientation can be written as:

$$\langle \mathbf{t}(s) \cdot \mathbf{t}(s + \ell) \rangle \simeq 1 - \langle \kappa^2 \rangle \ell^2 / 2 - \langle \partial_s \kappa^2 \rangle \ell^3 / 4 + \dots, \quad (7)$$

in contradiction with the simple exponential approximation. Here  $\kappa^2 = \partial_s \mathbf{t} \cdot \partial_s \mathbf{t}$  is the local curvature of the fiber. As this relation does not involve any physical properties of the fiber the same behavior is expected for polymer. Furthermore this relation enlightens the fact that the persistence length is a function of the local curvature of the fiber. This idea is already present in Brouzet *et al.* [2]. They explained that if the fiber length  $L$  is equal to the elastic length  $\ell_e$ , the correlation function should be equal to  $\sin \theta / \theta$ , where  $\theta = \ell / \ell_e$ . Indeed, when the fiber length is equal to the elastic length, the deformation is an arc of circle with radius  $R \geq \ell_e$ . Then, the correlation function is simply:

$$\mathbf{t}(s) \cdot \mathbf{t}(s + \ell) = \cos \ell / R. \quad (8)$$

The correlation function can be found by averaging over all configurations, *i.e.* from a straight line to an arc of circle of radius  $\ell_e$ :

$$\begin{aligned} \mathcal{C}(\ell) &= \langle \mathbf{t}(s) \cdot \mathbf{t}(s + \ell) \rangle \\ &= \frac{\ell}{L} \sin \frac{L}{\ell} = \frac{\ell_e}{\ell} \sin \frac{\ell}{\ell_e}. \end{aligned} \quad (9)$$

We have compared this prediction to our measurements in the inset of figure 5. We can see that the cardinal sine (dashed dotted line) fits very well the experimental curve with no adjustable parameters for  $\ell < 0.5\ell_e$ . Therefore, the Taylor expansion of the cardinal sine ( $\sin(x)/x \sim 1 - x^2/6$ ) gives a relation between the elastic length  $\ell_e$  and the mean curvature  $\langle \kappa^2 \rangle$ :

$$\langle \kappa^2 \rangle = \frac{1}{3\ell_e^2}. \quad (10)$$

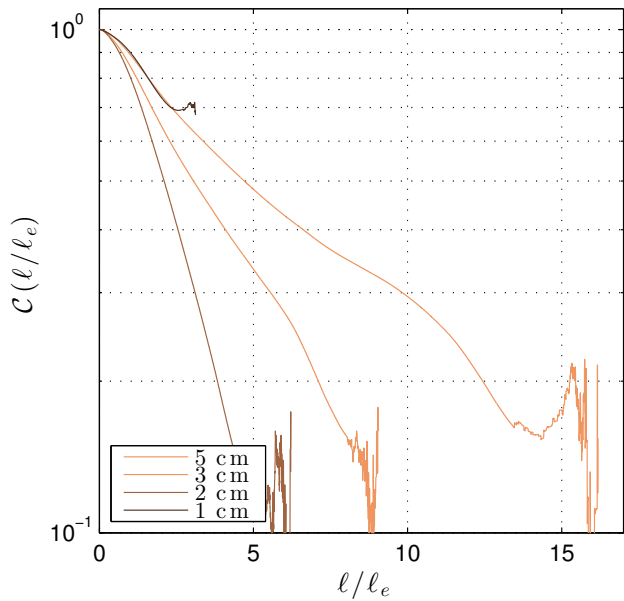


**Fig. 6** Evolution of the correlation length as a function of the fiber length.

We focus now on the evolution of the correlation function with the fiber length for the same elastic length  $\ell_e$ . We can see in figure 6 that the experimental curve does not superimpose for all lengths. Whereas the correlation functions overlap for the shortest and the longest fibers, they decrease more rapidly for intermediate lengths. This is in contradiction with the wormlike chain model which assumes that the correlation function depends only on the persistence length  $l_p$ . However, for long enough fibers ( $L > 1$  cm) two regimes are visible. For large  $\ell$ , the correlation function is nearly linear in a log-lin plot (see figure 6). So this part can still be modeled by an exponential law but with a characteristic length which depends also on the fiber length. For small  $\ell$ , the correlation function is still quadratic but the mean curvature  $\bar{\kappa} = (\langle \kappa^2 \rangle)^{1/2}$  changes with the fiber length. Then the fit with the cardinal sine seems to be valid only for the shortest and the longest fibers. The relation between the mean curvature and the elastic length does not hold for the intermediate lengths. An evaluation of  $\bar{\kappa}$  with the elastic length using equation (10) will underestimate the value by nearly 10 % for the 2 cm fiber.

As the shape of the correlation function varies with the fiber length in turbulence, the analogy between the deformations of a fiber in a turbulent flow and the distortions of a polymer submitted to thermal fluctuation is not rigorous. We may now wonder if this result could also have been observed without the 3D reconstruction tools we have developed.

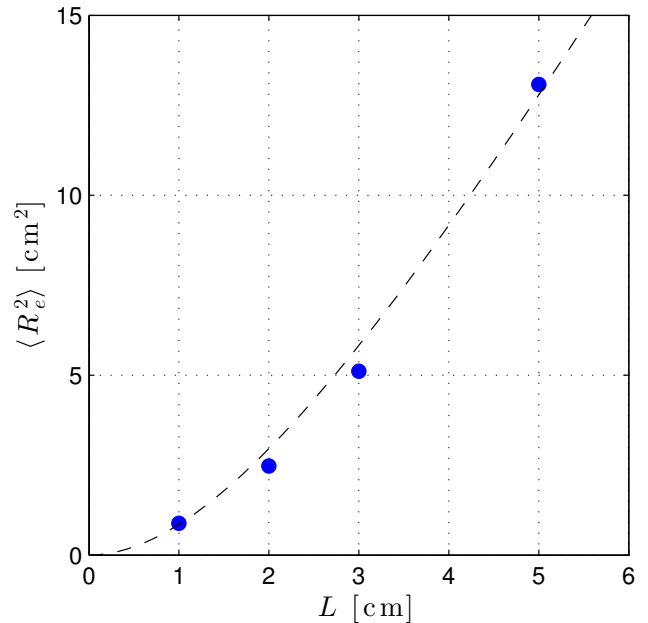


**Fig. 7** Mean value of the norm of the end to end vector  $\langle R_e^2 \rangle$  as a function of the fiber length. The blue dot is the measurement and the dashed line the best fit from the prediction of the wormlike chain theory. The uncertainty scales roughly with the symbol size.

In Brouzet *et al.*, the analogy was based on the non linear evolution of the norm of the end to end vector  $\langle R_e^2 \rangle$  when the fiber length is increased. The same quantity is presented in figure 7 where the measurement uncertainty is nearly the symbol size. The dashed line represents the best fit of the evolution of the norm of the end-to-end vector as a function of the fiber length, *cf.* equation (4), where the persistence  $l_p$  is considered here as a fit parameter and is noted  $l_{p,R_e}$  in the following. We can see here that with only this integral quantity it is difficult to assess the analogy between polymers and flexible fibers as the fit with  $l_{p,R_e} \simeq 6\ell_e$  is very close to the experimental points. The 3D reconstruction allows one to access local quantities, such as the correlation function, which are more sensitive and allowed us to clearly show that the fiber length plays an important role in the fiber deformation in turbulence contrary to wormlike chain polymer.

Note that in Brouzet *et al.* the persistence length was equal to  $2\ell_e$  and not  $6\ell_e$  as is the case here. This difference is not due to the difference of the experimental techniques used in both studies but is related to the flow correlation. Indeed, in turbulence the flow is correlated at scale  $r$  smaller than the so called integral scale  $L_I$  with a correlation  $\mathcal{C}_t(r) \sim r^{2/3}$ . As the elastic length is here 10 times smaller than in our previous study, the turbulent fluctuations at the origin of the deformation do not have the same correlation. Then it is expected

that the relation between the persistence length and the elastic length differs in both studies. Beyond the polymer analogy, this observation opens new perspectives to model the fiber deformation in turbulence which appears to be a very rich problem.

## 5 Conclusion

In this study we used the classical epipolar geometry to determine fiber conformations in a turbulent von Kármán flow. The measurement of the correlation function of the orientation of the tangent vector along the fiber shows that the analogy between flexible fibers distorted by turbulent fluctuations and wormlike chain polymers submitted to thermal fluctuations is not always true. In both cases, the correlation function  $\mathcal{C}(s)$  is proportional to  $1 - (\kappa^2)s/2$  for  $s \ll \ell_e$  and, for  $s \gg \ell_e$ , it can be approximated by an exponential law  $\exp(-s/l_p)$ . However we showed that for flexible fibers, the persistence length is a function of both the elastic length  $\ell_e$  and the fiber length  $L$  whereas it depends only on the elasticity for polymers. This dependence on the fiber length is directly related to the flow correlation, which is scale-dependent in turbulence.

The relation between the flow properties and the fiber statistics deserves to be studied in more details. As is shown by equation (7), there is a direct relation between the correlation function and the local curvature. A better understanding on the physics of the deformation might be possible by investigating the curvature statistics and the tools developed here can be easily adapted to this task. Finally, the measurement of fiber deformations might allow one to determine some flow properties. For instance, the estimation of the persistence length for very long fibers seems related to the flow integral scale. It is also possible to estimate the turbulent dissipation rate  $\epsilon$  by looking at the correlation function for short distances. Indeed, by fitting the correlation function with a quadratic function, it is possible to estimate the elastic length  $\ell_e = (EI)^{1/4}/(\rho\eta\epsilon)^{1/8}$  within 10 %. This gives  $\epsilon$  within a relatively large range as it can be overestimated by a factor of 2. This kind of measurement could however be useful in oceanography as it allows a rapid estimation of the local dissipation rate.

## References

1. Bouguet, J.Y.: Camera calibration toolbox for Matlab. URL [http://www.vision.caltech.edu/bouguetj/calib\\_doc/](http://www.vision.caltech.edu/bouguetj/calib_doc/)
2. Brouzet, C., Verhille, G., Le Gal, P.: Flexible fiber in a turbulent flow: a macroscopic polymer. *Phys. Rev. Lett.* **112**(7), 074,501 (2014)
3. Byron, M., Einarsson, J., Gustavsson, K., Voth, G., Mehlig, B., Variano, E.: Shape-dependence of particle rotation in isotropic turbulence. *Phys. Fluid* **27**, 035,101 (2015)
4. Chari, V., Sturm, P.: Multi-view geometry of the refractive plane. *Proc. British Machine Vision Conf.* (2009)
5. Chevillard, L., Meneveau, C.: Orientation dynamics of small triaxial-ellipsoidal particles in isotropic turbulence. *J. Fluid Mech.* **737**, 571–596 (2013)
6. Faugeras, O., Luong, Q.T., Papadopoulos, T.: *The Geometry of Multiple Images*. MIT Press (2001)
7. Hartley, R.I., Sturm, P.: Triangulation. *Comput. Vis. Image Und.* **68**(2), 146–157 (1997)
8. Hartley, R.I., Zisserman, A.: *Multiple View Geometry in Computer Vision*. ISBN: 0521540518. CUP (2003)
9. Hinch, E., Leal, L.: Rotation of small non-axisymmetric particles in a simple shear flow. *J. Fluid Mech.* **92**(3), 591–608 (1979)
10. Jarecki, L., Blonski, S., Blim, A., Zachara, A.: Modeling of pneumatic melt spinning processes. *J. Appl. Polym. Sci.* **125**, 4402–4415 (2012)
11. Jeffery, G.: The motion of ellipsoidal particles immersed in a viscous fluid. *Proc. R. Soc. Lond. A* **102**, 131–179 (1922)
12. Lee, I.K.: Curve reconstruction from unorganized points. *Comput. Aided Geom. D.* **17**(2), 161–177 (2000)
13. Longuet-Higgins, H.: A computer program for reconstructing a scene from two projections. *Nature* **293**, 133–135 (1981)
14. Lopez-Caballero, M.: Large scales in a von Kármán swirling flow. Ph.D. thesis, University of Navarra (2013)
15. Lundell, F., Soderberg, L., Alfredsson, P.: Fluid mechanics of papermaking. *Annu. Rev. Fluid Mech.* **43**(1), 195–217 (2011)
16. Machicoane, N., Zimmermann, R., Fabiane, L., Bourgoïn, M., Pinton, J.F., Volk, R.: Large sphere motion in a nonhomogeneous turbulent flow. *New J. Phys.* **16**(1), 013,053 (2014)
17. Machicoane, N., Zimmermann, R., Fabiane, L., Bourgoïn, M., Pinton, J.F., Volk, R.: Large sphere motions in a nonhomogeneous turbulent flow. *New J. Phys.* **16**(1), 013,053 (2014)
18. Macnab, R., Koshland, D.: The gradient sensing mechanism in bacterial chemotaxis. *Proc. Natl. Acad. Sci. U.S.A* **69**, 2509–2512 (1972)
19. Maier-Hein, L., Groch, A., Bartoli, A., Bodenstedt, S., Boissonnat, G., Chang, P.L., Clancy, N.T., Elson, D.S., Haase, S., Heim, E., Hornegger, J., Jammin, P., Kenngott, H., Kilgus, T., Müller-Stich, B., Oladokun, D., Röhl, S., dos Santos, T.R., Schlemmer, H.P., Seitel, A., Speidel, S., Wagner, M., Stoyanov, D.: Comparative validation of single-shot optical techniques for laparoscopic 3D surface reconstruction. *IEEE Trans. Med. Imaging* **33**(10), 1913–1930 (2014)
20. Marchioli, C., Soldati, A.: Rotation statistics of fibers in wall shear turbulence. *Ata Mech.* **224**, 2311–2329 (2013)
21. Marcus, G., Parsa, S., Kramel, S., Ni, R., Voth, G.: Measurement of the solid body rotation of anisotropic particles in 3d turbulence. *New J. Phys.* **6**, 102,001 (2014)
22. Marheineke, N., Wegener, R.: Fiber dynamics in turbulent flows: General modeling framework. *SIAM Journal on Applied Mathematics* **66**(5), 1703–1726 (2006)
23. Miralles, S., Bonnefoy, N., Bourgoïn, M., Odier, P., Pinton, J.F., Plihon, N., Verhille, G., Boisson, J., Daviaud, F., Dubrulle, B.: Dynamo threshold detection in the von Kármán sodium experiment. *Phys. Rev. E* **88**(1), 013,002 (2013)
24. Ouellette, N., Xu, H., Bourgoïn, M., Bodenschatz, E.: Small-scale anisotropy in lagrangian turbulence. *New J. Phys.* **8**, 102 (2006)
25. Parsa, S., Calzavarini, E., Toschi, F., Voth, G.: Rotation rate of rods in turbulent fluid flow. *Phys. Rev. Lett.* **109**, 134,501 (2012)

26. Powers, T.: Dynamics of filaments and membranes in a viscous fluid. *Rev. Mod. Phys.* **82**(2), 1607 (2010)
27. Pumir, A., Wilkinson, M.: Orientation statistics of small particles in turbulence. *New J. Phys.* **13**, 093,030 (2011)
28. Ravelet, F.: Bifurcations globales hydrodynamiques et magnétohydrodynamiques dans un écoulement de von Kármán. Ph.D. thesis, CEA Saclay (2005)
29. Rousset, B., Bonnay, P., Diribarne, P., Girard, A., Poncet, J.M., Herbert, E., Salort, J., Baudet, C., Castaing, B., Chevillard, L., Daviaud, F., Dubrulle, B., Gagne, Y., Hébral, M.G.B., Lehner, T., Roche, P.E., Saint-Michel, B., Mardion, M.B.: Superfluid High REynolds von Kármán experiment. *Rev. Sci. Inst.* **85**, 103,908 (2014)
30. Toschi, F., Bodenschatz, E.: Lagrangian properties of particles in turbulence. *Annual review of fluid mechanics* **41**, 375–404 (2009)
31. Treibitz, T., Schechner, Y., Kunz, C., Singh, H.: Flat refractive geometry. *IEEE Transaction on pattern analysis and machine intelligence* **34**(1), 51–65 (2012)
32. Trujillo-Pino, A., Krissian, K., Alemán-Flores, M., Santana-Cedrés, D.: Accurate subpixel edge location based on partial area effect. *Image and Vision Comput.* **31**(1), 72–90 (2013)
33. Voth, G., Porta, A.L., Crawford, A., Alexander, J., Bodenschatz, E.: Measurement of particle accelerations in fully developed turbulence. *J. Fluid Mech.* **469**, 121 (2002)
34. Yamakawa, H.: *Modern Theory of Polymer Solutions*. Harper and Row (1971)
35. Zimmermann, R., Gasteuil, Y., Bourgoïn, M., Volk, R., Pumir, A., Pinton, J.F.: Tracking the dynamics of translation and absolute orientation of a sphere in a turbulent flow. *Rev. Sci. Inst.* **82**(3), 033,906 (2011)

**Acknowledgements** This work has been carried out in the framework of the Labex MEC Project (No. ANR-10-LABX-0092), of the A\*MIDEX Project (No. ANR-11-IDEX-0001-02), funded by the “Investissements d’Avenir” French Government program managed by the French National Research Agency (ANR). A. Bartoli was funded by the FP7 ERC research grant 307483. Authors want to thanks B. Favier and P. Le Gal for fruitful conversation.